Demonstration of Literal Three-Dimensional Imaging

C. Ho, K.L. Albright, A.W. Bird, J. Bradley, D.E. Casperson, M. Hindman,
W.C. Priedhorsky, W.R. Scarlett, R.C. Smith, J. Theiler, S.K. Wilson

Los Alamos National Laboratory
Mail Stop D436, Los Alamos, NM 87545

(Accepted for publication in Applied Optics, 1998)

Abstract:
In a recent paper, a new technique was proposed for remote ranging and topographical mapping using a single photon-counting detector system and low power pulsed laser. This paper reports the results of laboratory and field demonstration of this literal three dimensional imaging technique. Using a detector system developed at Los Alamos with a commercial pulsed laser and observing from a single remote vantage point, we have demonstrated the viability of this technique in the literal mapping of three dimensional topography and probing of complex scene. With a reasonably short exposure, this system can resolve features with height variation as small as 5 cm.

Keywords: lidar; photogrammetry; laser ranging; photon-counting; remote sensing; lasers, applications

I. Introduction

In a recent paper by Priedhorsky, Smith and Ho[1], we described a technique where a high resolution photon counting imaging system is used to remotely measure the three dimensional topography of a target scene. This three dimensional imaging concept is based on the ability to measure, accurately and absolutely, the position and time of arrival for individual photon. Suppose we illuminate a scene with a light source containing a known time signature such as periodic sharp laser pulses and observe remotely with a photon sensor system that offers both high spatial and time resolution. The detected photons come either from the random background or from the reflection from the scene of the illumination. The background photons do not have any embedded time signature, whereas the reflected photons from the illumination will retain the known time signature. By performing a correlation with the time signature, we can significantly enhance the signal over the background. Use of narrow band filter in conjunction with a laser will allow us to further reduce the background contribution. In the end, we can obtain high quality three dimensional *(x,y,t)* information even under conventionally low signal-to-background condition. Just like in a conventional lidar, the arrival time of the photons is translated directly to range.

Combined with the imaging capability of the system, the data acquired with this technique yields the literal three dimensional profile of the target scene.

As discussed in Priedhorsky et al., this technique opens many new applications as well as offers great advantages over existing sensor systems. In its simplest form, this technique allows us to derive the relative topography of solid objects in the scene from a single remote vantage point. A large area high accuracy survey of ground topography can be achieved from an airborne platform using a low power laser, which would be a great advantage over existing scanning lidar altimeter. Furthermore, the scattering property and distribution of a complex three dimensional structure can be probed with this system. For example, this technique can be used to study the multiple scattering and radiation transfer properties of a cloud (Davis, Ho, and Love[2]). Another application is the measurement of distribution of plant leaves as three dimensional suspended objects. Issues such as biomass in a forest or plant health could be addressed by such measurements.

Since mid-1997, an end-to-end system with the capabilities needed for this literal three dimensional imaging technique has been in operation. To fully demonstrate this novel three dimensional imaging technique, we have conducted a number of experiments both in the laboratory and in the field. The ability and accuracy of three dimensional imaging depends primarily on the available photon statistics and only secondarily on the absolute distance to the target scene. In this paper, we report the results of two experiments at two different observing distances using the same low power laser, a laboratory experiment observing an artificial target from a distance of 6 m, and a field experiment observing a natural scene from a distance of 50 m. These results quantitatively demonstrate the concept of remote literal three dimensional imaging. The organization of this paper is as follows. In section II, we discuss the laboratory experiment, data processing and analysis, and the results. To help explain the concept, we have adopted a pedagogical approach in the analysis section. Section III describes the field experiment and the results. A summary and discussion is given in Section IV.

II. Laboratory Experiment and Results

II.a Experimental Setup

The experiment consists of the following major components: a dark laboratory, a pulsed laser as the illumination system, the target, light collecting optics, and most importantly, the MicroChannel Plate/Crossed Delay Line detector with Pulse Absolute Timing electronics

(MCP/CDL/PAT) sensor system. We describe the characteristics of individual components in the following:

Laboratory: The experiment was conducted in a dark laboratory with an overall length of about 7 m. The laboratory can be made relatively dark with some minor light sources. Through the use of narrow band filter as described below, the ambient light was reduced to a manageable level. An optical table was located at one end of the room where the illumination and observing subsystems were attached. The target was placed at the other end of the laboratory at a distance about 6 m from the sensor system. The schematics of the experiment is shown in figure 1.

Target: A target was constructed from a block of 5-cm thick Styrofoam™ (open cell expanded polystyrene foam). Four block letters, LANL, were carved from the Styrofoam block with line thickness of about 1.5 to 2 cm. The four letters were glued to a 30 by 50 cm Styrofoam block of the same 5 cm thickness. The base Styrofoam block was attached vertically to the wall. Figure 2 shows a picture of the target where the letters can be distinguished based on the shadows.

Illumination system: As described in Priedhorsky et al., this technique requires active illumination with known timing characteristics. For this experiment, we used a Hamamatsu PLP-01 solid state laser that is externally triggered at 1.5625 MHz and synchronized to the reference 100 MHz clock of the PAT electronics described below. The laser head emits 83 ps light pulses at 655 nm with a peak power of 54 mW: At 640 ns pulse period, the average power is about 7 µW. The laser output beam shape is highly asymmetric. To achieve a more uniform illumination, we coupled the laser to a 120 µm diameter 7-m long multi-mode optical fiber. The divergence of the beam at the exit of the optical fiber is about 45 degrees. A lens was placed in front of the fiber exit to help concentrate the light to the target area.

Light collecting optics: We used an Orion Maksutov-Cassegrain 500 mm f/5.6 telescope to collect the light. The collection optics and the illumination system are roughly collocated on the same optical table. A imaging quality narrow-band filter centered at 655 nm with a 10 nm bandpass was placed behind the telescope and immediately in front of the detector. The target block was focussed and centered at the detector's active sensing area.

MCP/CDL/PAT: The MCP/CDL detector is a hermetically sealed vacuum tube made by Photek Ltd. (UK) under a contract from Los Alamos National Laboratory. The tube uses S-20 photocathode material for light sensing. Through a triple stack of 40 mm diameter MCPs arranged in a chevron fashion (a Z-stack), each excited photoelectron is intensified by a factor of about 10^7. The resulting charge cloud is read out by a crossed delay line anode with two orthogonal layers of helical conducting wires (Williams, Sobottka, and Shepherd[3]; Baron and Priedhorsky[4]). Each layer of wire has two ends and each photon event will generate electrical pulses at all four ends. The position and time of the photon event is determined by measuring the relative and average pulse arrival time of the four pulses from the same photon event. This is achieved by acquiring the data through a fast timing system, the PAT electronics, which contain four channels referenced to a common clock. Each channels are triggered independently by the four readouts of the crossed delay line anode. The current PAT system is implemented on industry-standard VME architecture and contains four separate PAT channels commonly referenced to a stable100 MHz clock. Each PAT channel contains custom analog-to-digital circuits which measures the absolute timing of individual electrical pulse with a resolution of 2.44 ps. The independent measurement of the arrival time of the four pulses allows us to reconstruct the photon event through an algorithm based on coincidence constraint, discriminating between two simultaneous events.

To date, we have achieved the following performance in the laboratory. The best full-width-half-maximum (FWHM) of a point source measured through the end-to-end MCP/CDL/PAT system is 60 μm. The timing accuracy for each photon is about 200 ps rms or 420 ps FWHM. We expect the current implementation to offer linear response up to a random count rate of about 10^6 counts/sec before significant event degradation occurs due to coincidence. For the literal 3D imaging field and laboratory experiments, the system has slightly degraded spatial and timing performance from the numbers above. As we continue to improve the system, we expect a point-source FWHM better than 30 μm, an absolute timing FWHM of about 100 ps, and a maximum count rate of 5×10^6 counts/sec. A more detailed description and performance of the MCP/CDL/PAT system will be given elsewhere.

Experiment: The experiment was conducted under the dark conditions described above. To control the data acquisition and perform quick-look analysis, we used two notebook computers in the same laboratory. The detector has a dark count rate about 600 counts/sec over its entire active area. Through the narrow band filter, the ambient light, which included the reflected light from the two computer screens, contributed about another 600 counts/sec. The reflected laser light contributed about 1200 counts/sec. With an overall count rate of about 2400 counts/sec, the system's capability was significantly under-utilized. A number of data sets were acquired under the same conditions at 240 seconds exposure each. Data were stored as raw pulse arrival time series from each channel for post facto processing and analysis. We note that the same exposure can be performed in less than 1 second with a laser of 3 mW average power which would yield about 5×10^5 counts/sec.

II.b. Data Processing, Analysis and Results

Taking at face value the breakdown of various contributions to the count rate, one would conclude that the signal-to-background ratio of the laser illumination in the data set is 1:1. Under normal circumstances, such signal-to-background ratio would contain limited useful information content. However, the high accuracy timing information for each photon coupled with the usage of the pulsed laser allows us to perform straightforward timing analysis to separate the signal from the background. Through the timing analysis, the background is effectively removed. The data processing and analyses are performed in the following standardized steps:

1. Raw data are processed into photon events;
2. Photon events are time-analyzed to establish correlation of the laser return photons;
3. Random background is reduced through phase selection; and
4. Topography information is calculated from the data.

Step 1. Photon event construction: The raw timing data sets are processed through the photon event construction step based on a coincidence algorithm which is a key aspect of the MCP/CDL/PAT system. Under the current implementation, each exposure will yield four associated data sets, each containing an independent time series, $\{x1\}$, $\{x2\}$, $\{y1\}$, and $\{y2\}$. Each of the time series has a high precision and high dynamic range: The time is recorded as an integer in units of 2.4414 ps with a dynamic range of 58 bits. Out of the four independent time series, valid photon events are constructed by

$$x = x1\text{-}x2, \tag{1a}$$

$$y = y1\text{-}y2, \tag{1b}$$

$$t = (x1+x2+y1+y2)/4, \tag{1c}$$

where the coincidence constraint must be satisfied for each event:

$$d = |(x1+x2)-(y1+y2)| < \delta. \tag{1d}$$

The width of the coincidence widow δ is small, currently measured to be about a few hundred picoseconds. This stringent constraint offers the capability of discriminating between two simultaneous but not collocated photon events, leading to an effective detector dead time of a few tens of nanoseconds. This step yields a list of photons recorded as the event position and time (x,y,t) at the detector's sensing surface. High precision timing analysis can be performed over the entire exposure. In the rest of this paper, we discuss the analyses and results of one four-minute exposure.

We extract the data set which contains 256 by 256 pixels with each pixel covering an area of about 150 microns square at the detector's surface. This maps a pixel of 1.8 mm square at the target with the field of view (FOV) covering about 45 cm square. Figure 3a shows a *negative* image constructed from the full data set. The circular area is defined by the detector's active area. The four corners of the FOV in the data space, devoid of photons, do not map to the detector's active area. The edges of the detector's circular active area, on the other hand, have been truncated in this format. There are several notable features in this image: 1) The two dark stripes (light intensity corresponding to low counts) at the top and bottom are the black optical tapes used to attached the Styrofoam block to the wall. 2) The two bright spots in the upper half of the image are caused by specular reflection of the laser from a metallic electrical wall panel which was not fully covered by the black tape. 3) The bright spots in the middle of the FOV and the upper right corner are hot spots that have developed inside the tube. Unlike figure 2, one cannot see the letters LANL in Figure 3 through either intensity contrast or shadow.

Step 2. Time analysis: As described in Priedhorsky et al., the fact that the target scene was illuminated by a source with a known time signature allows us to separate the laser return photons from the random background. The time-random background include the intrinsic detector dark count, the ambient light, and the hot spots in the detector. These background photons have a random arrival time and no correlation with the laser pulse period. In contrast, the returned laser photons retain the time signature of the pulsed laser. To distinguish photons with random and periodic time signature, we construct a secondary photon list where the time for each photon is the 'phase' of the photon's arrival time relative to the periodicity. Specifically, the secondary photon list (x,y,t') is related to (x,y,t) by

$$t' = (-t + dt_{\mathrm{F}} + dt_{\mathrm{I}}) \text{ modulo } P, \qquad \text{where } P = 640 \text{ ns.} \tag{2}$$

Without loss of generality, we intentionally use the negative value of t to calculate t' such that the calculated phase maps directly to topography as if we are looking from the top: photons with larger t' are reflected from a location closer to the observer. In equation (2), we introduce two correction terms dt_{F} and dt_{I} to remove various sources of curvature in the observed field. First, as described in Priedhorsky et al., geometry dictates that photons reflected from different parts of the FOV travel different distances between the illumination source and the detection. To correct this field curvature, we apply a correction factor

$$dt_{\mathrm{F}} = T_F[\sec(\theta)-1], \tag{3}$$

where θ is the angle of the photon's registered position relative to the center of the FOV, and T_F is the round trip time for photons detected at the center of the FOV, which we have taken to be 40 ns over the distance of 6 m. Second, photons emerging from the optical fiber at different angles have different propagation path length through the fiber. This leads to a strong dependence of the timing on the exit angle. In a way, the laser pulse is broadened. To correct for the 'curved illumination front', we apply a second correction factor

$$dt_I = T_I[\sec(\kappa\theta)-1]. \qquad (4)$$

The normalization factor T_I is taken to be 35 ns for the propagation time of the photons along the fiber, after taking into account the fiber's index of refraction. The factor κ is introduced to account for the light concentrating lens. For this analysis, we take κ=2. In this formalism, we are making the implicit assumption that the illumination and observing system are collocated. As discussed below, the quality of the results indicates that the collocation assumption is reasonable. Figure 4a shows the phase distribution over the full range of 640 ns for the entire data set which contains about 571,000 photons. Most of the phase range contains an average of about 24 counts per 48.8-ps phase bin. This distribution is obviously dominated by a sharp feature at 438 ns: the highly correlated laser return bearing the pulse signature.

Step 3. Phase culling: With the sharply peaked phase distribution near 438 ns, we construct a culled data set which contains only those photons with a phase in the range of 434 to 440 ns. They are predominantly returned laser light. The image from the culled data set is shown in Figure 3b. The main difference between the Figure 3a and 3b is the absence of the hot spots at the center and the edge of the FOV, which do not have any time signature. Figure 4b shows the distribution of the phase-culled data set containing about 288,000 photons. We estimate the random background to contribute about 2900 photons within the 6 ns phase range. Thus the signal-to-background ratio in the culled data set is about 100:1. The peak is fully resolved with a FWHM of 680 ps, slightly greater than, yet consistent with the best achieved time accuracy discussed above. There is no strong evidence of any complex structure in figure 4.

Step 4. Topography extraction: The phase-culled data set is processed by the simple topography determination algorithm outlined in Priedhorsky et al. We construct a local phase distribution around each pixel based on the photons falling within an n by n pixel region centered around the pixel in question. For this analysis, we take n=3. The median of the localized phase distribution is designated as the pixel's 'range': Multiplying by a factor of $c/2$, with c being the speed of light, the range maps directly to the topographical height. Figure 5 shows the calculated topographical map: Figures 5a to 5c show the topographical map as an intensity map, contour plot and surface plot, respectively. It is obvious that we have resolved the 5 cm height separation between the LANL letters and the solid Styrofoam block. The flatness of the topographical images, most visible in figures 5a and 5b, indicates the absence of significant residual field curvature, and confirms the validity of various assumptions and correction terms used in the analysis.

To further characterize the system performance, we plot the distribution of calculated heights for the ensemble of pixels in figure 6. The distribution is clearly multi-modal. Three broad yet distinct peaks are seen near 20, 25, and 30 cm, which we identify as the wall, the flat surface of the solid Styrofoam base, and the letters LANL, respectively. The height difference matches the thickness of the building material of the target: standard two inch (5 cm) thick Styrofoam blocks available in the local hobby stores. In this figure, pixels with fewer than 2 counts, including the four corners in the images shown in figure 3, have been assigned a height of 17 cm, shown as the sharp peak at the said location.

We now compare these results with the theoretical expectation. The average count per pixel in the culled data set is about 4. The local phase distribution used to calculate the height would typically contain 36 counts from 9 pixels. Given the high signal-to-background ratio of the culled data set, it is reasonable to assume that the distribution follows normal statistics dictated by the single photon timing accuracy. Suppose we use 680 ps FWHM shown in figure 3 as the underlying time accuracy for individual photons. We estimate that the mean/median can be determined to an accuracy of about 680 ps/$(36)^{1/2}$ ~ 110 ps FWHM. This corresponds to an estimated FWHM for the distribution of calculated height of about 1.7 cm. Literal measurement around the peak at 25 cm in figure 6 gives a FWHM of about 2.8 cm. Keeping in mind that we have applied two correction factors and the topography extraction algorithm is not truly local, we consider this height determination accuracy to be in reasonable agreement with the simple theoretical estimate. This again confirms the validity of the time correction terms used in equations (3) and (4). For example, if these corrections were not applied, the curved field would incur a discrepancy at the edge of the FOV of order of 270 ps or 4 cm, which would have been readily apparent in the height map or distribution.

III. Field Experiment and Results

III.a. Experimental Setup

The field experiment follows the same principle and setup as the laboratory experiment. Below, we briefly review the field experiment setup with emphasis on the differences between the field and laboratory experiments.

Field setup: We conducted the field experiment in a local canyon. The entire illumination and observing system was located in a self-contained recreational vehicle which was parked on a paved road in the middle of the canyon. The vehicle was about 50 m away from the foot of the canyon wall where the target was situated. The experiment was performed under a moonless condition.

Target: In addition to the natural scene at the foot of the canyon wall, we placed a 3 foot cubical wooden box in the target scene. The box was painted with a black-and-white checkerboard pattern as shown in Figure 7. To simplify the analysis and data interpretation, we covered the box with solid yellow color carpet during the experiment. Figure 7 clearly shows that the box was located on a sloped ground and leaning slightly forward.

Illumination: We used the same pulsed laser externally triggered at 1.5625 MHz. For this experiment, we chose to directly use the beam out of the laser head without the intervening fiber. As a result, illumination of the scene was not uniform but without the illumination curvature (cf. Eq[4]).

Optics and *MCP/CDL/PAT:* These subsystems were essentially identical to the configuration used in the laboratory experiment.

Experiment: Data were acquired following the standard procedures. Over the entire detector area, the detector dark count was about 600 counts/sec, and the scene contributed about 800 counts/sec through the narrow band filter under the moonless condition. The laser return accounted for about 1500 counts/sec.

III.b. Analysis and Results

In this section, we describe the results of a 200-second exposure taken in the field experiment. The data processing follows the standardized procedures described in section II.b, with the exception that we have not applied the topography determination algorithm.

After constructing the photon events, we perform the time analysis following equation (2). For this data set, the illumination front correction term, dt_I, is not applied because we used the laser output directly in the experiment. Photons from a roughly 3.8 m square region at the target location are extracted from the data set with 256 by 256 pixels in the spatial dimension. This data set contains about 494,000 photons. The phase distribution over 640 ns is shown in figure 8a. Compared to figure 4a, figure 8a exhibits much more complicated structures. The features in the range of 250 ns to 350 ns (corresponding to a distance range of about 15 m) can be identified as various foreground objects. Among the foreground objects were tall weeds in the canyon floor that contribute to the lower portion of the FOV. In this paper, we concentrate on the time period between 220 and 245 ns. The phase distribution is shown in figure 8b. The phase-culled data set contains 74,000 photons with about 10,000 photons from the random background.

The phase culled data set contains photons distributed in a volume with a size of about 3.8 m on each side. The resolution in each dimension is 1.5 cm or better. This allows us to perform direct visualization of the data. Figure 9 shows the projected images of this data cube along the three axes separately: the front, top and side views.

In the front view, we can distinguish the box in the lower left quadrant after consulting the other views. The two front surfaces are more prominent than the top surface because of the more favorable reflection angle. This view has a band-like structure which is understood as follows. Because of the sloped ground, foreground and background objects cover lower and upper portion of the image respectively. The selection of a viewing depth of 3.8 m excludes photons reflected from foreground and background objects, leaving only those photons within the right depth range to contribute to the image in a band.

The dominant feature in the top view is the "V" pattern in the lower left corner which is the projection of the two front surfaces of the box. The "V" pattern has a finite width estimated to be about 1.5 ns (or 22 cm). This is greater than the FWHM of single photon timing distribution, estimated earlier to be about 680 ps FWHM under field operation condition. Close inspection reveals that this width is dictated by the forward leaning of the box on the sloped ground which is easily seen in the side view as well as in figure 7. In this view, we can also see a void of photons behind the box. This is the shadow of the laser illumination due to the blockage by the box.

The side view clearly shows the sloped ground and the restricted height range due to the selected depth range. One can see the variation of the sloped ground. In addition, there is a diffuse distribution of photons above the ground, which is the result of the reflection of the ground vegetation in the scene as seen in figure 7.

The three views shows the power of this technique. Data generated by this system literally maps the three dimensional structure of the target scene which can be directly visualized without extensive and extraneous data processing.

IV. Discussions and Summary

In these experiments, the phase difference between the laser pulse and photon time series was arbitrarily fixed for each data set. Except for the correction term dt_F, relative topographical map is derived without explicit determination of the absolute distance. As discussed in section II.b, the height determination accuracy can be predicted by the photon statistics which is determined by the laser power, distance, and exposure time. Bearing in mind that these experiments used a very low power laser and significantly under-utilized the capabilities of the MCP/CDL/PAT system, we do not foresee any difficulty in achieving the system performance in the remote sensing scenarios of large observing distances discussed In Priedhorsky et al.

The knowledge of the absolute distance is required to correctly apply the field curvature compensation factor in equation (2). As stressed by Priedhorsky et al., built-in to this concept is a ranging ambiguity of $cP/2$ (96 m for 640 ns pulse period). For an observing distance smaller than $cP/2$, it is straightforward to determine the absolute phase difference of the illumination and the laser return. For measurements with a distance greater than $cP/2$, we can either employ a conventional ranging system to supply the information or perform self-consistent algorithmic determination of the range by examining the observed field curvature.

A comparison between the raw image (e.g. figure 3) and the topographical image (e.g. figure 5) demonstrates the power of this technique: This technique remotely measures the literal three dimensional profile of the target with a short exposure from a single vantage point. Compared to existing remote 3D probing schemes such as synthetic aperture radar and scanning lidar, this scheme offers the following advantages:

this system uses a low power eye-safe laser;

this system has low weight and power requirements as described in Priedhorsky et al.;

this system has neither moving parts nor stringent alignment requirements;

this system offer simultaneous coverage over a wide area in short exposures; and

the data are literally three dimensional and do not require extraneous data processing.

As discussed earlier, the essence of this technique is to measure the three dimensional distribution of return photons from a scene under a directed illumination. The distribution of the return photons maps literally to the reflecting or back scattering elements in the observed scene. Even though the experiments reported in this paper were performed for solid targets with contiguous surfaces, it is straightforward to apply this technique to measure reflecting objects suspended in three dimension or even more complex three dimensional structures.

To summarize, we have demonstrated the concept of imaging the three dimensional profile of a remote target using single photon counting detector and active illumination. We envision many applications for this new technique.

Acknowledgments: This work was performed under the auspices of US Department of Energy. CH thanks Lauren and Karen Ho for their assistance in the construction of the Styrofoam target.

References

1. Priedhorsky, W. C., Smith, R. C., and Ho, C., "Laser ranging and mapping with a photon-counting detector," *Applied Optics,* **35**, 441-452 (1996).
2. Davis, A. B., Ho, C., and S.P. Love, S. P., "Off-beam (multiply-scattered) lidar returns from stratus, 2: space-time measurements in a laboratory simulation," in *Proc. 19th International Laser Radar Conference Proceeding*, U. Singh, S. Ismail, and G. Schwemmer, eds., 55-58, 1998, Annapolis (Md), NASA Center for Aero-Space Information (CASI).
3. Williams, M.B., Sobottka, S.E., and Shepherd, J.A., "Delay line readout of MicroChannel Plates in a prototype position-sensitive photomultiplier tube", *Nuclear Instruments and Methods in Physics Research*, **A302**, 105-112 (1991).
4. Baron, M. H., and Priedhorsky, W. C., "Crossed delay line detector for ground and space based applications," in *EUV, X-Ray and Gamma-Ray Instrumentation for Astronomy IV*, O.H. Siegmund, ed., Proc. Soc. Photo-Opt. Instrum. Eng. **2006**, 188-197 (1993).

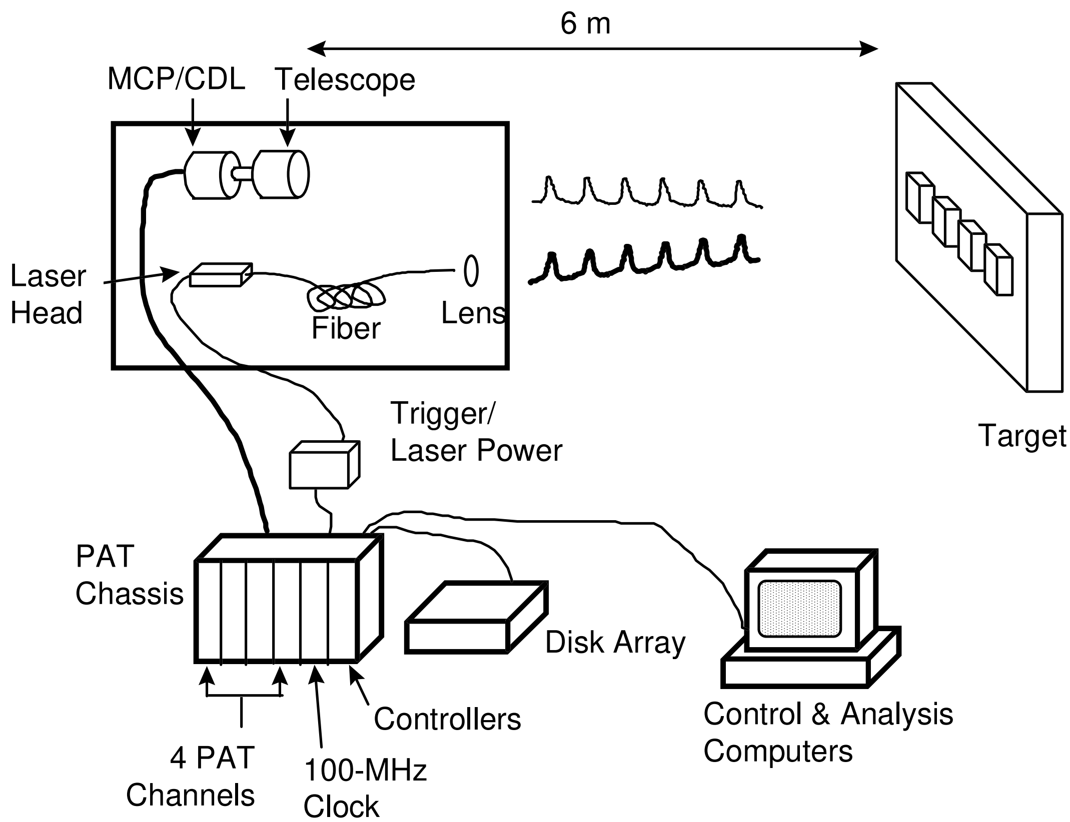

Figure 1. Schematics of the laboratory experimental setup. The entire experiment is contained in a 24-ft long dark laboratory. See text for detailed discussion of individual subsystems.

Figure 2. Styrofoam target used in the laboratory experiment.

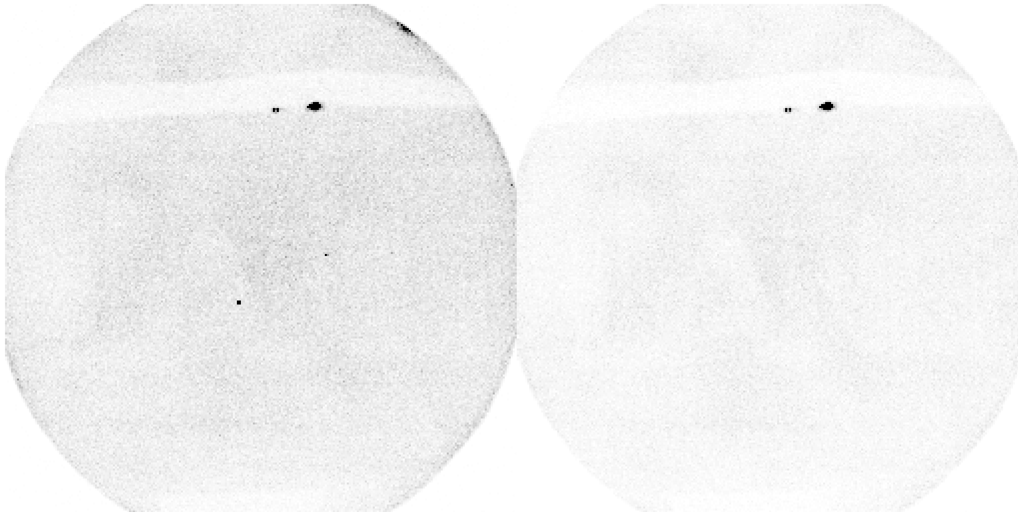

(a) (b)

Figure 3. Images of the target scene from the laboratory experiment. The intensity map is shown as the negative, i.e. darker pixels contains more counts. Figure 3a gives the image constructed from the total data set. The features are described in the text. Figure 3b is constructed from the phase-culled data set which contains about half of the number of photons of the image in figure 3a. In additional to being dimmer than figure 3a, figure 3b also lacks the hot spots at the center and upper right corner of the FOV. They are randomly distributed in time and suppressed by the phase culling.

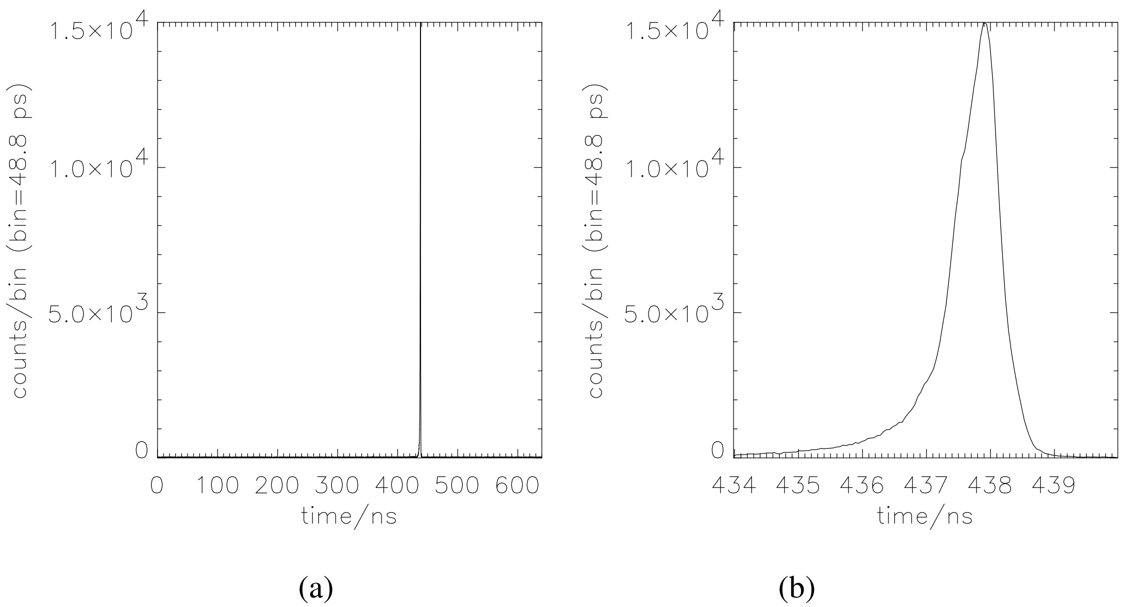

Figure 4. Phase distribution of the photon list. Figure 4a shows the overall distribution of the calculated phase from 0 to 640 ns. The dominant feature at 438 ns is shown in greater details in figure 4b.

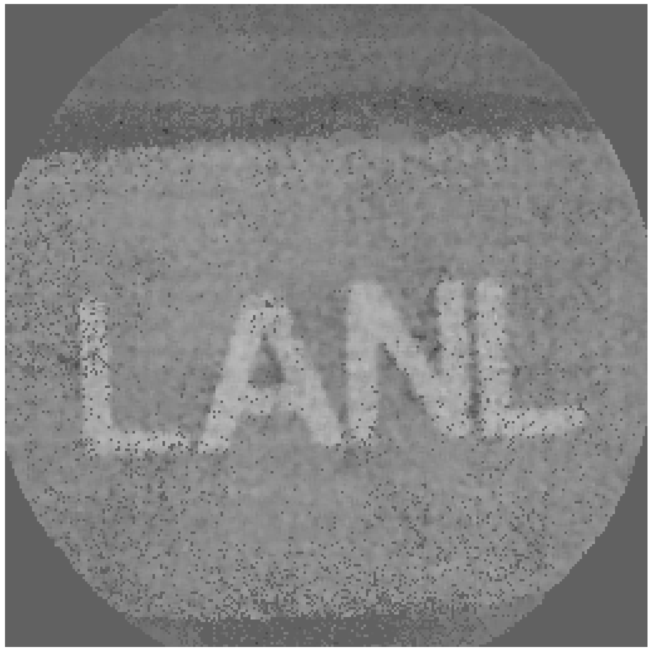

(a)

Figure 5a. Calculated topographical map of the target as a positive intensity map. Brighter pixels have greater height, or are closer to the observer.

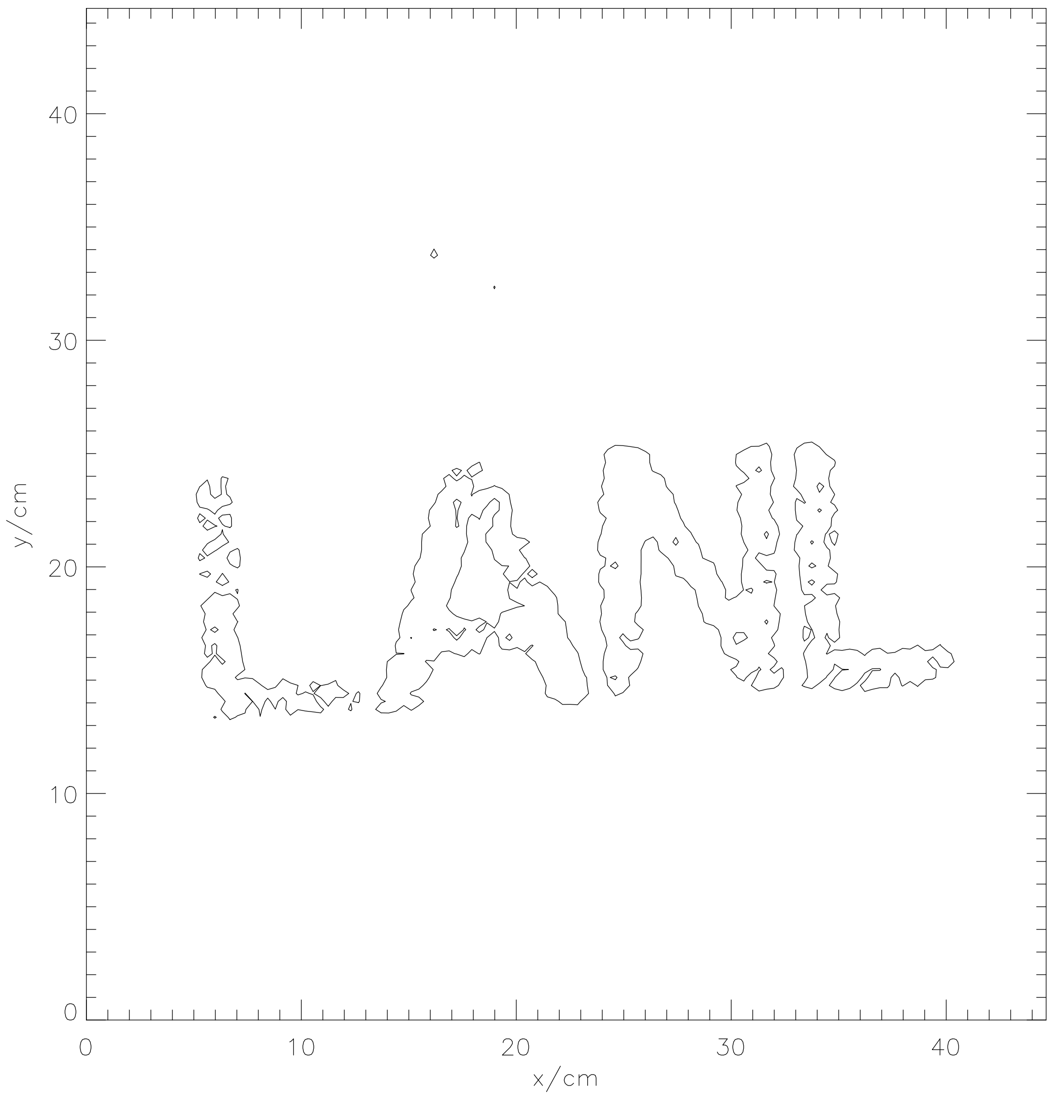

(b)

Fig. 5b. Contour map of the calculated topography. To reduce confusion, only one contour level at 27.5 cm (cf. fig. 6) is imposed.

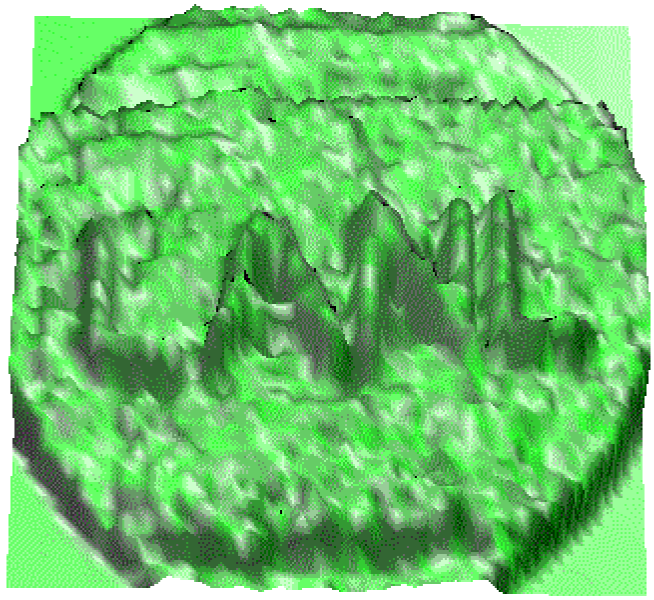

(c)

Fig. 5c. Calculated topography shown as a surface plot viewed from a slightly oblique angle. In this visualization, ‘lighting’ effect are employed to form shadow.

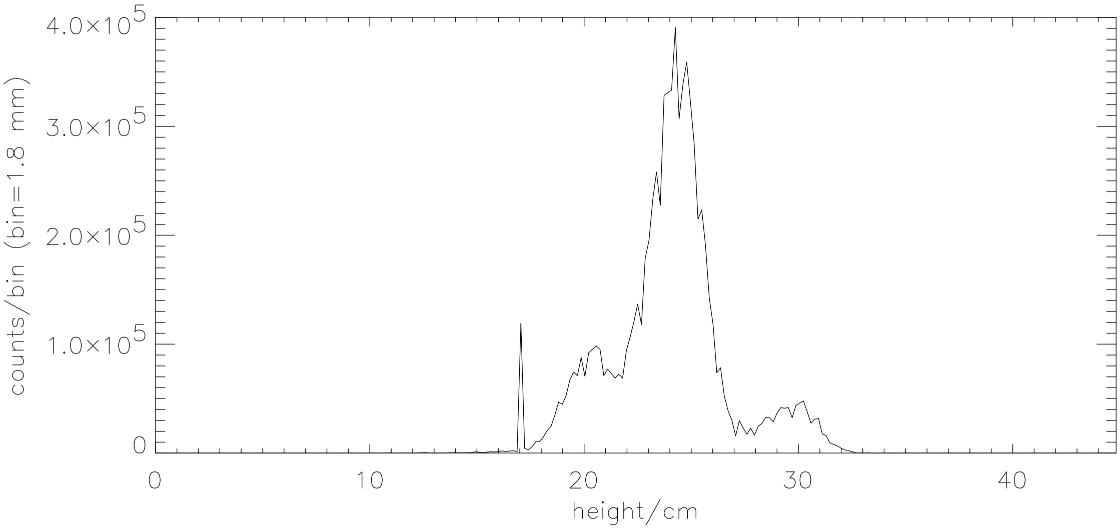

Figure 6. Distribution of the calculated height. The distribution is clearly multi-modal. We identify the features at 20, 25 and 30 cm as the wall, the solid Styrofoam block and the letters LANL. The sharp feature at 17 cm is the assigned height of the pixels with less than 2 counts. These are the dark pixels in figure 5a.

Figure 7. The three-feet cube wooden box target used in the field experiment. A solid yellow color carpet was used to cover the entire box during the experiment. Notice the sloping of the ground and forward leaning of the box.

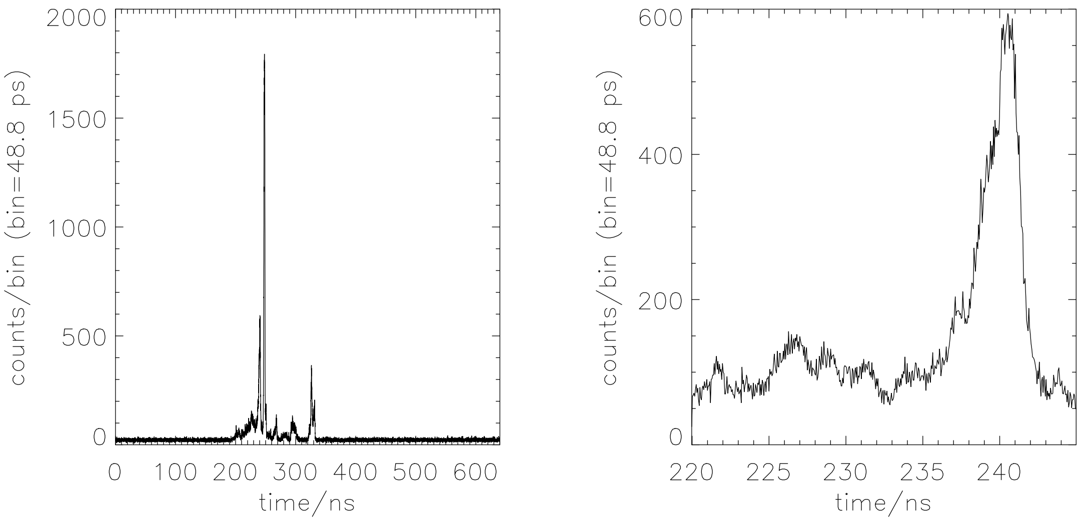

(a) (b)

Figure 8. Phase distribution of the field experiment data set. Figure 8a shows the full 640 ns range where complex structures are easily seen. Figure 8b shows the range between 220 and 245 ns.

Top View

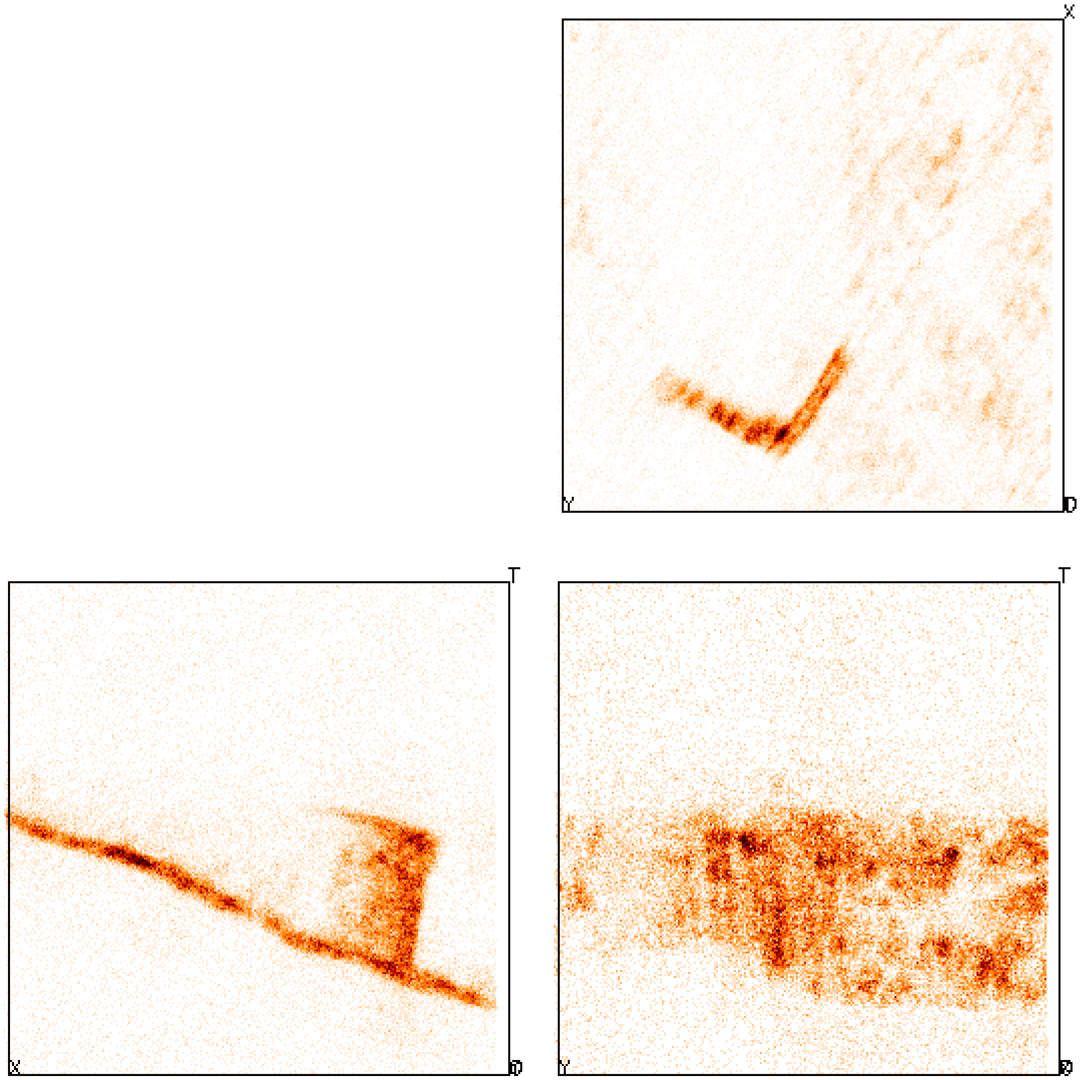

Side View

Front View

Figure 9. The 3D data box shown as negative images projected from different viewing angle. The labeling of the 3D Box is as follows: +T axis is up; +Y is to the left viewing from the front; and +X is along the line of sight away from the observer. See text for more detailed discussions.